ACS NANO

www.acsnano.org

ARTICLE

Amorphous Carbon Monolayer: A van der Waals Interface for High-Performance Metal Oxide Semiconductor Devices

Viswanath G. Akkili,[¶] Jongchan Yoon,[¶] Kihyun Shin,[¶] Sanghyun Jeong, Ji-Yun Moon, Jun-Hui Choi, Seung-Il Kim, Ashish A. Patil, Frederick Aziadzo, Jeongbeen Kim, Suhyeon Kim, Dong-Wook Shin, Jung-Sub Wi, Hoon-Hwe Cho, Joon Sik Park, Eui-Tae Kim, Dong-Eun Kim, Jaeyeong Heo, Graeme Henkelman, Kostya S. Novoselov, Choong-Heui Chung,* Jae-Hyun Lee,* Zonghoon Lee,* and Sangyeob Lee*

Cite This: *ACS Nano* 2025, 19, 1056−1069

Read Online

ACCESS | Metrics & More | Article Recommendations | Supporting Information

ABSTRACT: **Ultrasmall-scale semiconductor devices (≤5 nm) are advancing technologies, such as artificial intelligence and the Internet of Things. However, the further scaling of these devices poses critical challenges, such as interface properties and oxide quality, particularly at the high-*k*/semiconductor interface in metal-oxide-semiconductor (MOS) devices. Existing interlayer (IL) methods, typically exceeding 1 nm thickness, are unsuitable for ultrasmall-scale devices. Here, we propose a one-atom-thick amorphous carbon monolayer (ACM) as the IL to address these issues for MOS devices. ACM is disordered, randomly arranged, and short of long-range periodicity with sp^2 hybridized carbon network, offering impermeability, van der Waals (vdW) bonding, insulating behavior, and effective seeding layer. With these advantages, we have utilized ACM vdW IL (vIL) in Al_2O_3/H−Ge MOS capacitors. The interface trap density was suppressed by ∼2 orders of magnitude to 7.21 × 10^{10} cm^{-2} eV^{-1}, with no frequency-dependent flat band shift. The slow trap density is decreased to 2 orders of magnitude, and the *C*−*V* hysteresis width is minimized by >75%, indicating enhanced oxide quality. These results are supported by high-resolution transmission electron microscopy and energy dispersive X-ray spectroscopy analysis, confirming the creation of an atomically well-defined interface in the Al_2O_3/H−Ge heterojunction with ACM vIL, even under high-temperature annealing conditions. Density functional theory calculations further clarify that ACM vIL preserves the hydrogen-passivated Ge surface without altering its electronic band structure. These results demonstrate that ACM vIL effectively improves the interface properties and enhances the oxide quality, enabling further advancements in ultrasmall-scale MOS devices.**

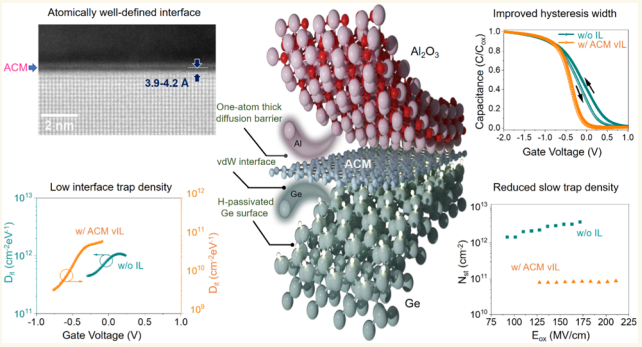

KEYWORDS: *amorphous carbon monolayer, semiconductor interface, interface trap density, MOS capacitors, MOS interlayer*

Technological advancements in the semiconductor industry have driven a continuous reduction in device dimensions (*e.g.*, reaching ≤3 nm process nodes), ensuring the validity of Moore's law. This technological trend aligns with the predictions of the international roadmap for devices and systems-2023 (IRDS), which forecasts the node range of logic devices to reach 1.5 nm by 2028 and 1 nm by 2031.[1] The metal-oxide-semiconductor (MOS) structure has been the heart of semiconductor devices, and has been simultaneously scaled down with the devices, and the high-*k* oxide thickness has been reduced to ≤2 nm.[2] However, several issues have arisen in this ultrasmall-scale regime to enhance device performance. Among them, the oxide quality and interface properties, specifically the oxide/semiconductor interface in MOS field effect transistors (MOSFETs), are critical issues. The properties of the MOS device are mainly

Received: September 11, 2024
Revised: December 9, 2024
Accepted: December 17, 2024
Published: December 31, 2024

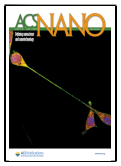

https://doi.org/10.1021/acsnano.4c12780
ACS Nano 2025, 19, 1056−1069

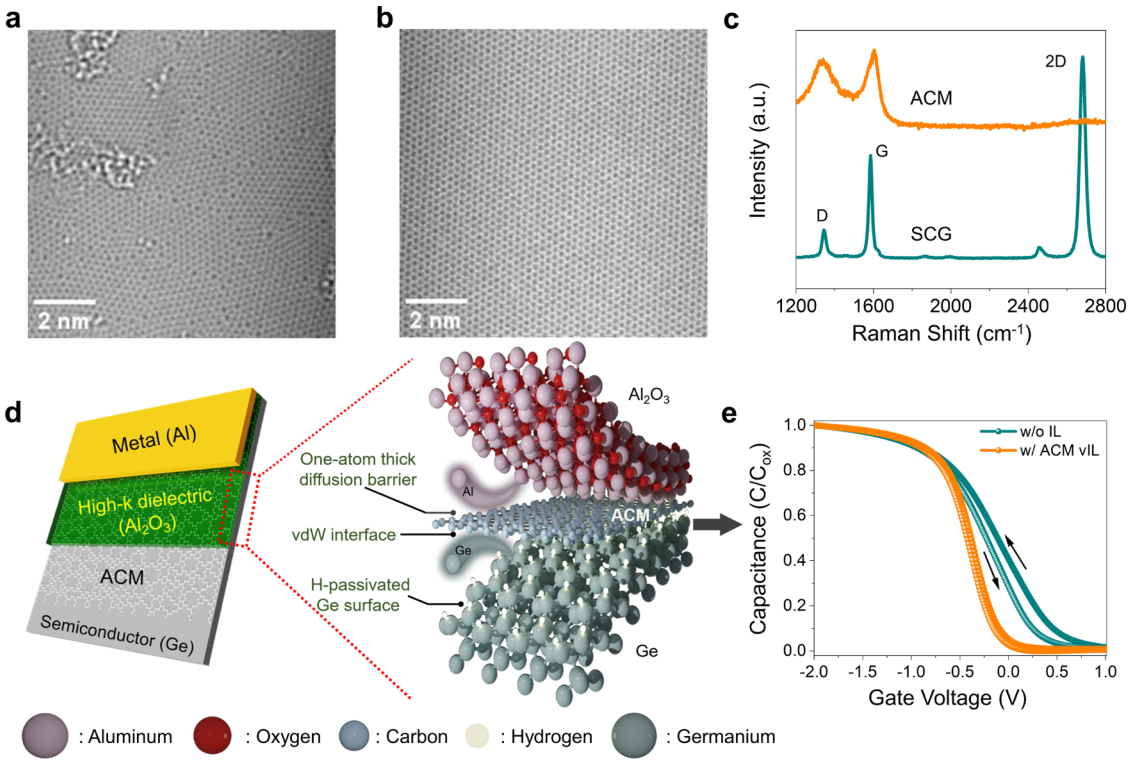

Figure 1. Structure and functional role of the ACM as a vIL. Plan-view HR−TEM image of the (a) ACM and (b) SCG at scale of 2 nm. Unlike the uniform structure of the SCG, the ACM reveals a heterogeneous blend of randomly arranged pentavalent, hexavalent-, and octavalent carbon rings with a short-range of periodicity. (c) Raman spectra of the ACM and SCG, revealing distinct structural features. The 2D peak disappeared in the ACM (vivid orange line) spectra, indicating the amorphous nature and lack of long-range periodicity. (d) Schematic illustration of a cross-sectional view of the Al/Al_2O_3/ACM/H−Ge structure. The enlarged portion highlights the concept of the ACM as vIL elucidating the features of the passivation of H−Ge, prevention of Al and Ge atoms interdiffusion, and establishment of the vdW interface between H−Ge and Al_2O_3 layers. (e) Normalized *C*−*V* characteristics of the w/ACM vIL (pumpkin patch color), compared to the w/o IL configuration (dark cyan color). The reduction in the hysteresis reveals the decrease in oxide traps near the Al_2O_3/H−Ge interface via ACM vIL.

governed by charges and defects within the oxide,[3−5] and traps present in interface states at the oxide/semiconductor junction.[6] Charges within the oxide can be incorporated during the fabrication process, and via interdiffusion at heterojunction between high-*k* oxide and semiconductor materials.[4,5] Similarly, interface trap states can be generated by the defects and surface reconstruction on semiconductor surfaces.[7]

To resolve these issues in MOS devices, particularly those based on Si, next-generation Ge and III−V compound semiconductors, various process technologies, materials, and layer structures have been explored. Process techniques, such as plasma-post oxidation,[8] electron cyclotron resonance preplasma oxidation,[9] and forming gas annealing[10,11] have been implemented to enhance device performance. Recently, hydrocarbon materials[12] and ferroelectric materials, such as $HfZrO_2$,[13] HfO_2−ZrO_2,[14] and $Hf_{0.5}Zr_{0.5}O_2$[15] have emerged as alternatives to replace the conventional gate oxides with higher-*k* values, thus decreasing gate thickness. Various interlayer structures at oxide/semiconductor junctions have been introduced to minimize interface trap density (D_{it}) and improve long-term stability by preventing interdiffusion during device operation. In Si−based devices, hydrogenation[16,17] and nitridation[18,19] strategies have been employed to prevent oxidation and reduce defects on semiconductor surfaces, leading to suppressing the formation of interface trap states. Similarly, for Ge and III−V semiconductors, approaches such as oxidation,[20] nitridation,[21] and the use of crystalline silicon interface layer (IL)[22] have been utilized to enhance interface quality.

Among these methods, ILs stand out as particularly effective in resolving issues associated with oxide and interface quality in ultrasmall-scale MOS devices, since they can conduct chemical passivation to reduce the D_{it}, and simultaneously serve as physical barriers to minimize interdiffusion. To fulfill this role effectively, ILs must possess an optimal thickness to ensure chemical stability, thereby acting as a reliable diffusion barrier. Yet, most ILs utilized in MOS capacitors (MOSCAP) have been relatively thick, exceeding 1 nm, attaining $D_{it,max}$ in the range of 10^{11} cm^{-2} eV^{-1}.[23−25] The best reported $D_{it,max}$ value for a Ge MOSCAP was 4.5×10^{10} cm^{-2} eV^{-1},[26] achieved using a thick GeO_x IL of 4 nm. The incorporation of such thick ILs can induce shifts in flat band voltage (V_{FB}), series resistance, and overall gate capacitance, affecting the MOS device performance[2] and posing considerable challenges to the advanced downscaling of MOS devices.

One potential solution to these challenges could be adapting a one-atom-thick two-dimensional (2D) material as an IL. We propose an amorphous carbon monolayer (ACM) as the IL in MOS devices. ACM is disordered, randomly arranged, and short of long-range periodicity with an sp^2 hybridized carbon network.[27,28] The structure of ACM can be readily compared with its counterpart single crystal graphene (SCG), as shown in Figure 1a,b. The disordered nature of ACM is further

https://doi.org/10.1021/acsnano.4c12780
ACS Nano 2025, 19, 1056−1069

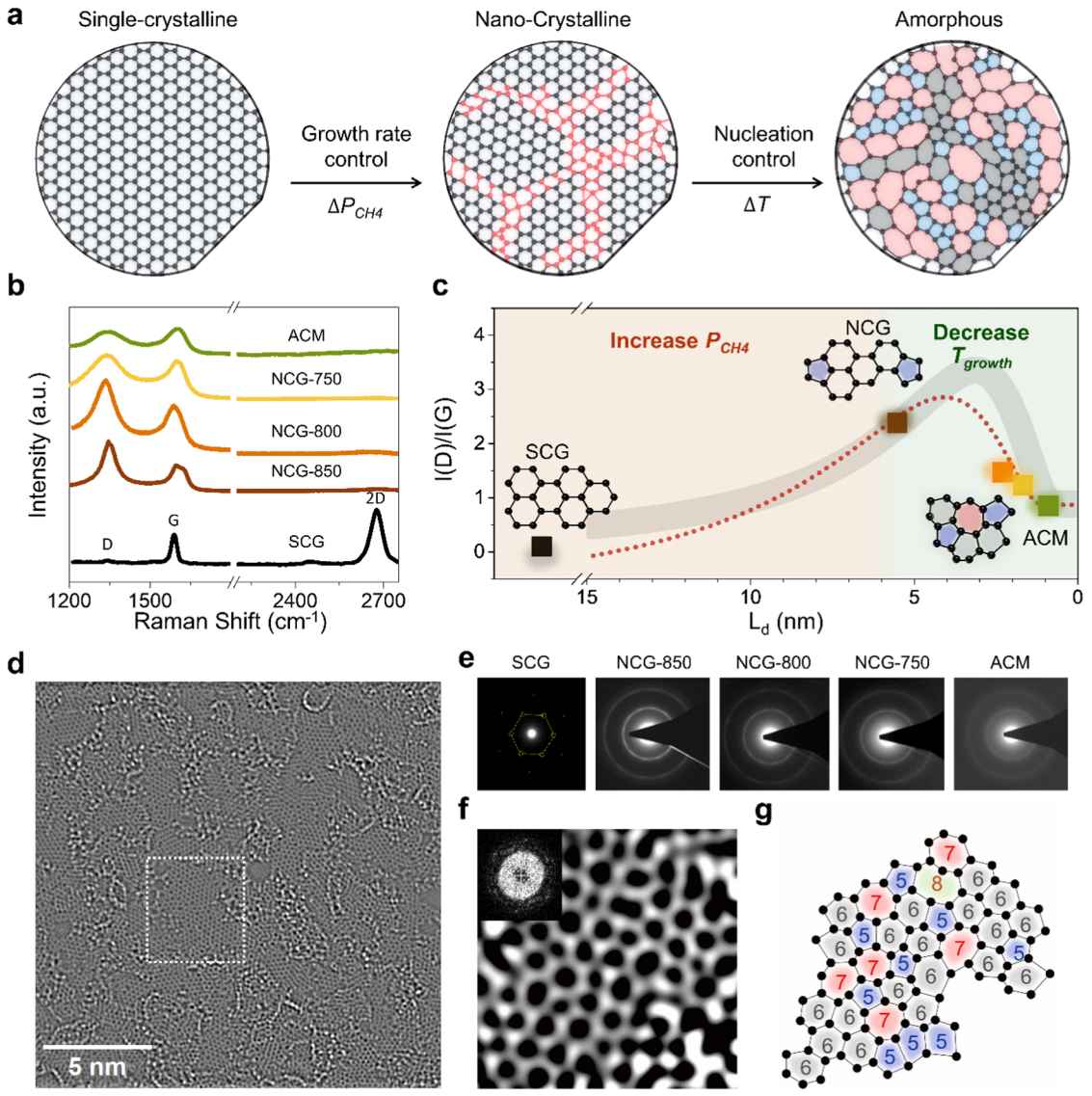

Figure 2. Direct synthesis of ACM via growth parameter tuning. (a) Schematic illustration of the catalytic growth of single crystalline, nanocrystalline, and amorphous carbon monolayer structures. (b) Raman spectra depicting the transition from single crystalline to amorphous structure of graphene samples synthesized under various conditions. (c) Optimal growth conditions for the ACM achieved by controlling synthetic parameters P_{CH4} and T_{growth}. The data points for $I(D)/I(G)$ of different samples synthesized under various conditions are extracted from (b). The solid gray line represents the plot of the $I(D)/I(G)$ as a function of L_d, based on the equation from ref (53), while the dashed red line is the fitted curve based on the experimental data. (d) Atomic-level structure of the ACM grown on the H–Ge(100) at 700 °C synthesis temperature. Unlike single crystalline graphene, it lacks structural periodicity. (e) SAED patterns of the SCG to ACM samples grown under different conditions. The ACM shows a diffused ring pattern with no diffraction spot. (f) Zoomed area of (d) displaying a distorted structure. (g) The distorted structure comprising a mix of pentagonal, hexagonal, and heptagonal carbon rings.

evident in the Raman spectra with the absence of a 2D peak at 2680 cm^{-1}, typically attributed to SCG, suggesting a lack of long-range periodicity[29] (Figure 1c). ACM offers four distinct advantages over other ILs: As a similar manner to its counterpart SCG, (i) ACM can be impermeable to all gases, except for hydrogen,[30] and exhibits high thermal and chemical stability[31] owing to its continuous sp^2 hybridized carbon network. Thus, it can act as a one-atom-thick diffusion barrier. The H atoms used for passivation are covalently bonded to Ge atoms, forming stable Ge–H bonds.[32−34] These H atoms are not in the form of free-standing H molecules or atomic H that could diffuse through the ACM layer; instead, they are chemically attached to the Ge surface, effectively terminating dangling bonds and passivating the surface. (ii) ACM generates van der Waals (vdW)[35] bonding on the surfaces of other materials, without noticeably altering the electronic properties of underlying semiconductor surfaces. After chemical processing of the semiconductor surface to minimize surface states and reconstruction, the vdW bonding of ACM effectively passivates semiconductor surfaces. In contrast to SCG, (iii) ACM exhibits Anderson's insulating behavior,[36,37] making it suitable for use as an IL in the oxide/semiconductor heterojunction in a MOSCAP. (iv) ACM can function as an effective seeding layer for subsequent overlayers to be grown and/or deposited. Its amorphous nature induces chemical potential undulation[38−40] on the surface, offering nucleation sites for overlayer growth.[41,42] Thus, high-k oxide can readily grow on ACM IL during MOS fabrication, as evidenced by

https://doi.org/10.1021/acsnano.4c12780
ACS Nano 2025, 19, 1056−1069

uniform wetting behavior resulting in a continuously grown Al_2O_3 layer (Figure S1b) on ACM surface. In contrast, the Al_2O_3 on SCG shows discrete island growth (Figure S1a). We previously reported the method to synthesize the ACM at a high temperature (>900 °C) with a controlled growth rate, revealing a highly disordered structure lacking long-range periodicity.[27] However, the scope of the study was limited to the synthesis process and basic material property characterization. In this work, we introduce an investigation, demonstrating significant advancements in the amorphous nature and insulating properties through the establishment of a low-temperature chemical vapor deposition (LP−CVD) process. The improved amorphous nature results in a sheet resistance value of ∼5 orders of magnitude higher than that of SCG (Figures S2−S4), consistent with the values reported by Tian et al.[28] These findings demonstrate that ACM exhibits Anderson's insulating behavior, which is crucial for its function as an IL material, preventing short-circuiting and maintaining the integrity of semiconductor device. We employ the Ge MOSCAP as our model system to validate the concept of using ACM as vdW IL (vIL). Ge, known for its superior electron and hole mobility, as well as low operating voltages,[43] has been studied as a next-generation channel material in MOSFETs. Yet, the chemically unstable Ge oxide readily grows on the Ge surface,[44,45] causing the generation of defects at the dielectric/Ge interface, which results in high D_{it} values in Ge MOSCAPs.[46] This limitation has been the main hindrance to the widespread industrial adaptation of Ge-based technologies. Several IL approaches, such as Ge surface passivation, multiple IL stack, and thick ILs have been applied to minimize D_{it}. A comprehensive list of IL structures and corresponding device performances is summarized in Table S1. With the aforementioned four key advantages, ACM can effectively resolve these challenges. The Ge MOSCAP with ACM vIL (termed w/ACM vIL) is depicted in Figure 1d, with an enlarged portion illustrating the effect of ACM vIL. The Ge surface is hydrogen-passivated (H−Ge) to suppress the surface reconstruction and defects, thereby maintaining the bulk electronic band structure and preventing Fermi energy level pinning at the interface.[39,47,48] ACM preserves the H−Ge via vdW bonding and effectively prevents the diffusion of Al atoms into the Ge and *vice versa*, thereby preserving both the interface and oxide quality. Empirical evidence of ACM vIL effectiveness, shown in Figure 1e, demonstrates a 75% reduction in hysteresis width and a shift in V_{FB} toward negative voltage, substantiating its role in mitigating oxide traps. In the subsequent sections of this article, a detailed analysis of the impact of ACM vIL on H−Ge MOSCAP is provided using capacitance−voltage ($C-V$) and conductance−voltage ($G-V$) electrical characterizations, along with the supporting structural characterizations. Furthermore, density functional theory (DFT) calculations are performed to evaluate the electronic band structure of the H−Ge(100) and ACM/H−Ge(100) surfaces.

RESULTS AND DISCUSSION

Direct Growth of the ACM on the H−Ge (100) Surface. To fabricate the w/ACM vIL, we directly synthesize ACM on the H−Ge(100) surface, since the Ge substrate has sufficient catalytic activity to form a sp^2 carbon network and its extremely low carbon solubility.[49−51] Carefully tuning the synthetic conditions, such as the partial pressure of methane gas (P_{CH4}) and a growth temperature (T_{growth}), allows effective control over nucleation density and growth rate. This synthetic optimization enables the achievement of ACM with a Debye length (L_d) of <1 nm being realized, as depicted in Figure 2a. Initially, the crystallinity of the as-synthesized graphene was modulated from single crystalline to nanocrystalline structure by employing high nucleation and fast growth with increased P_{CH4}. Figure 2b shows representative Raman spectra of graphene samples synthesized under different P_{CH4} with varying T_{growth}. The Raman spectra of SCG synthesized at low P_{CH4} exhibited typical features of large domain and high-quality graphene, with a negligible D peak (black line in Figure 2b). Conversely, as P_{CH4} increased, obtained graphene samples displayed a pronounced D peak and a decreased 2D peak (brown line in Figure 2b). Additionally, the D' peak, representing intravalley phonon scattering, began to emerge.[52] The intensity ratio of $I(D)/I(G)$ was calculated at ∼2.4, indicating the synthesis of nanocrystalline graphene (NCG) with an average grain size of ∼5 nm, as shown in Figure 2c, which represents $I(D)/I(G)$ as a function of L_d.[53]

To synthesize the desired ACM, adjustments were made to T_{growth}. In an H_2-containing atmosphere, high-temperature processes above 850 °C selectively etch away the chemically unstable defects in the carbon layer, thereby restricting the synthesis of ideal amorphous carbon sheets.[54] Therefore, efforts were directed toward identifying optimized conditions to minimize nanocrystalline grain size and synthesize ACM with a random network structure by lowering the synthesis temperature. The Raman spectra of samples synthesized under fast growth conditions (high P_{CH4}) with reduced T_{growth} are represented by orange, yellow, and green solid lines in Figure 2b, corresponding to T_{growth} values of 800, 750, and 700 °C, respectively. As T_{growth} was reduced below 850 °C, the 2D peak disappeared completely. For samples synthesized at 800 and 750 °C, extracted $I(D)/I(G)$ values of 1.47 and 1.23 indicated the presence of NCG with average grain sizes of 2.3 and 1.7 nm, respectively. Notably, the grain size of NCG gradually decreased as T_{growth} decreased. Upon further reduction of the synthesis temperature to 700 °C, an $I(D)/I(G)$ value of 0.85 was observed, signifying the synthesis of ACM with a grain size of <1 nm.[55,56] These results suggest that optimal growth conditions for ACM on H−Ge(100) were successfully attained by controlling synthetic parameters such as P_{CH4} and T_{growth} (Figures 2c, S5, and Figure S6).

To confirm the atomic-level structure of our ACM grown on the H−Ge substrate, high-resolution transmission electron microscopy (HR−TEM) was performed. Unlike SCG, which is free of structural defects, or nanocrystalline graphene, possessing high crystallinity within nanosized grains, ACM lacks structural periodicity (Figures 2d, and S7). Moreover, the selective-area diffraction patterns (SAED) of ACM show a ring pattern without any diffraction spot, which appears more diffuse compared to patterns from NCG samples grown under different conditions (Figure 2e). This observation suggests that ACM exhibits an amorphous feature. Figure 2f,g shows a zoomed-in view of Figure 2d, clearly displays the distorted structure comprising a mix of pentagonal, hexagonal, and heptagonal carbon rings.

Enhancement of Interface Properties and Oxide Quality: *C−V*, *G−V*, and *J−V* Analysis. To elucidate the impact of ACM as a vIL on the interface properties, multifrequency $C-V$ measurements were performed at room temperature on the Al_2O_3/p-Ge MOSCAP without an IL (termed w/o IL), and w/ACM vIL (Figure 3a,b). Gate

https://doi.org/10.1021/acsnano.4c12780
ACS Nano 2025, 19, 1056−1069

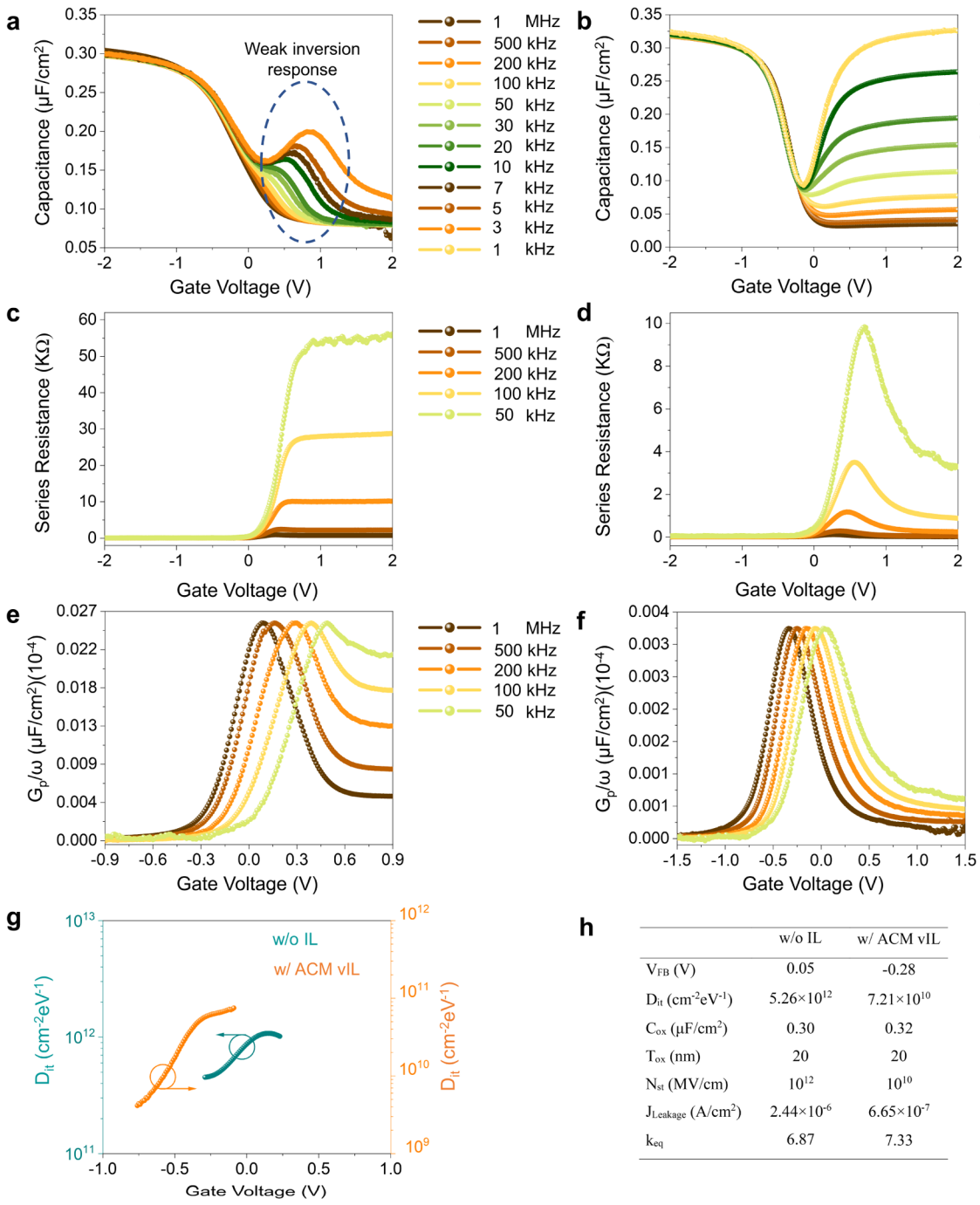

	w/o IL	w/ ACM vIL
V_{FB} (V)	0.05	-0.28
D_{it} ($cm^{-2}eV^{-1}$)	5.26×10^{12}	7.21×10^{10}
C_{ox} ($\mu F/cm^2$)	0.30	0.32
T_{ox} (nm)	20	20
N_{st} (MV/cm)	10^{12}	10^{10}
$J_{Leakage}$ (A/cm^2)	2.44×10^{-6}	6.65×10^{-7}
k_{eq}	6.87	7.33

Figure 3. Enhancement of interface trap states via the ACM vIL. (a) and (b) *C*−*V* characteristics of the w/o IL and w/ACM vIL, respectively, in the frequency range from 1 MHz to 1 kHz. The weak inversion response is highlighted in a, while it is eliminated in b with no shift in the frequency-dependent V_{FB}. (c) and (d) The variation of series resistance characteristics as a function of voltage from 1 MHz to 50 kHz in the w/o IL and w/ACM vIL, respectively. The series resistance is dramatically reduced in the w/ACM vIL. (e) and (f) Frequency-dependent normalized *G*−*V* characteristics from 1 MHz to 50 kHz in the w/o IL and w/ACM vIL, respectively. The magnitude of the conductance peak indicates the D_{it} value, which is minimized in the w/ACM vIL. (g) D_{it} spectra as a function of gate voltage, revealing a noticeable reduction by ∼2 orders of magnitude in the w/ACM vIL compared with the w/o IL. (h) Tabulation of the electrical properties of the w/o IL and w/ ACM vIL.

voltages (V_G) ranging from 2 to −2 V were applied to the devices, sweeping from inversion to the accumulation regimes at frequencies ranging from 1 MHz to 1 kHz. The w/o IL configuration exhibited a weak inversion response,[57] with a hump observed in the depletion and weak inversion region. However, incorporating the ACM vIL led to eliminating the weak inversion response. Moreover, the *C*−*V* slope became steep, with no frequency-dependent V_{FB} shift observed in the depletion region, indicating a reduction in D_{it}.[58] The V_{FB} values for w/o IL and w/ACM vIL were determined to be 0.05 and −0.28 V, respectively,[59] at a frequency of 1 MHz.

Quantitative analysis to extract D_{it} values includes various methods such as high−low *C*−*V*,[60] Terman,[61] frequency-dependent *G*−*V*,[62] deep-level transient spectroscopy,[63] and

https://doi.org/10.1021/acsnano.4c12780
ACS Nano 2025, 19, 1056−1069

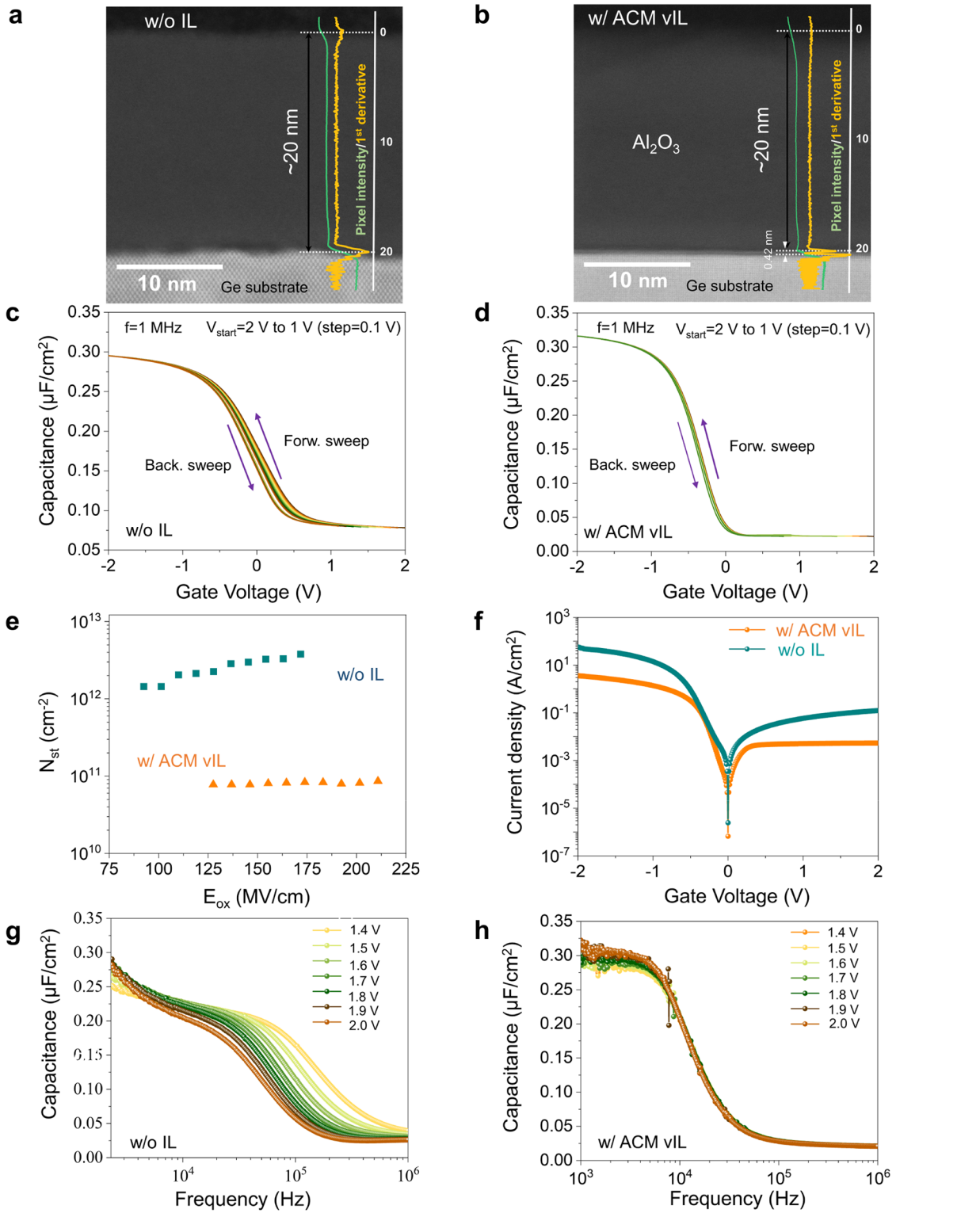

Figure 4. ACM vIL induced quality enhancement on oxide. (a) and (b) Cross-sectional STEM images of the w/o IL and w/ACM vIL. Both the devices exhibit an Al_2O_3 thickness of 20 nm, determined using the first derivatives of intensity profiles of ADF-STEM images. (c) and (d) Hysteresis characteristics of the w/o IL and w/ACM vIL, respectively. The V_{start} is varied from 2 to 1 V in steps of 0.1 V, while V_{stop} remains constant. (e) Relationship between the E_{ox} and N_{st} of the w/o IL and w/ACM vIL. The obtained N_{st} values for the w/o IL and w/ACM vIL are in the range of 10^{12} and 10^{10} cm^{-2}, respectively, indicating an enhancement in oxide quality. (f) Leakage current density spectra of the w/o IL and w/ACM vIL. The leakage current is reduced by 1 order of magnitude in the w/ACM vIL. (g) and (h) Capacitance with respect to frequency characteristics of the w/o IL and w/ACM vIL, respectively. The average value of the measured C_{ox} for the w/o IL and w/ACM vIL are 0.30 and 0.32 μF cm^{-2}, respectively, aligning with the $C-V$ measurements.

direct-current current−voltage[64] methods. Among these, the $G-V$ method is a direct approach for determining the interface defects of the device because the conductive loss in the depletion region is governed by the charging and discharging

https://doi.org/10.1021/acsnano.4c12780
ACS Nano 2025, 19, 1056−1069

of defects, and is therefore adapted in this work. An important parameter for obtaining accurate conductance is the series resistance.[6,65] Correcting the series resistance from measured parallel conductance values in the strong accumulation region can accurately isolate the interface state portion.[6] (Supporting Section 1 provides additional discussion on the series resistance to correct the conductance characteristics). The w/ACM vIL showed a notable reduction in the series resistance of the device, due to lower interface states,[66] measuring 160 Ω, compared to 950 Ω for the w/o IL configuration at 1 MHz (Figure 3c,d). Figure 3e,f show the corrected parallel $G-V$ characteristics of the w/o IL and w/ACM vIL configurations in the depletion to weak inversion regime with the measured series resistance. The conductive peak in the $G-V$ curves corresponds to the conductive loss of the devices, while the loss curves demonstrate typical interface state behavior.[62] The normalized height of the conductive peak in the w/ACM vIL configuration was 6.47 nF cm^{-2}, considerably lower than the 171.45 nF cm^{-2} in the w/o IL configuration, indicating lower D_{it} for w/ACM vIL. To quantify D_{it}, the conductance peak with a shoulder close to the high-frequency region was fitted using eq 1[67]

$$D_{it} = \frac{2.5}{Aq}\left(\frac{G_p}{\omega}\right)_{peak} \quad (1)$$

where A is the electrode area, q is the elementary charge, and $(G_p/\omega)_{peak}$ is the maximum value of the normalized conductance peak obtained for a given gate voltage. Figure 3g shows the extracted D_{it} spectra for both devices, with D_{it} limited to specific V_G values where a conductance peak is observed. The obtained $D_{it,max}$ values for the w/o IL and w/ACM vIL devices were 5.26×10^{12} and 7.21×10^{10} cm^{-2} eV^{-1}, respectively, revealing ~2 orders of magnitude decrease in D_{it}. Since D_{it} is extracted at a high-frequency region in the $G-V$ method, we employed another method, the capacitance method, which considers both low and high frequencies to calculate D_{it}. The D_{it} using the capacitance method is determined utilizing the equation provided below[68]

$$D_{it} = \left(\frac{C_{ox}C_{LF}}{C_{ox} - C_{LF}} - \frac{C_{ox}C_{HF}}{C_{ox} - C_{HF}}\right) \quad (2)$$

where C_{ox} is the oxide capacitance, C_{HF} is the capacitance at the high frequency, and C_{LF} is the capacitance at the low frequency. The $D_{it,max}$ values obtained were 6.45×10^{12} and 9.11×10^{10} cm^{-2} eV^{-1} for w/o IL and w/ACM vIL configurations, respectively. Although the calculated values are slightly higher than those extracted from the conductance method, the $D_{it,max}$ of the w/ACM vIL remains ~2 orders of magnitude lower than that of the w/o IL.

The dielectric layer thickness for both devices was precisely measured utilizing cross-sectional scanning transmission electron microscopy (STEM), as displayed in Figure 4a,b. Measurements from the STEM images indicated an identical thickness of ~20 nm for both devices. The ellipsometry analyses also confirmed thicknesses the same as 20.2 nm for the w/o IL and w/ACM vIL configurations, respectively. Despite the identical dielectric thicknesses, the w/ACM vIL device showed enhanced accumulation capacitance, increasing from 0.30 to 0.32 μF cm^{-2} with less dispersion, compared to w/o IL. Although the overall capacitance in the series configuration of C_{ox} and C_{ACM} (the capacitance of ACM) should decrease, an increase in overall capacitance is observed (a detailed explanation is provided in Supporting Section 2). This implies the enhancement of oxide quality grown on the ACM/H−Ge surface. To confirm the enhanced oxide quality on ACM vIL, we measured the slow trap densities (N_{st}) and gate leakage current.

Trap charges in the oxide, often referred to as slow trap states, are typically located in the nonstoichiometric oxides nearer to the interface. These trapped mobile charges primarily originate from bulk traps in the oxide layer,[69,70] border traps between the interfacial transition oxide and the oxide layer,[8,71] or both. Consequently, they lead to poor bias-temperature instability (BTI) characteristics[46,72] and hysteresis,[73,74] affecting the long-term reliability of the device. Besides oxide reliability, they diminish channel mobility in MOSFETs through Coulombic scattering and the loss of free carriers.[75] The characteristic method for probing these N_{st} values in oxides involves examining hysteresis in the $C-V$ characteristics as a function of the effective electric field (E_{ox}).[76,77] When voltage is applied across the device, charges are captured or released from the oxide traps, leading to a change in the magnitude of hysteresis upon the voltage sweep's direction change. The magnitude of this hysteresis is proportional to the number of charges trapped and released, which is referred to as N_{st} in oxides. eqs 3 and 4 are employed to quantify N_{st} vs E_{ox}

$$E_{ox} = (V_{min} - V_{FB})/CET \quad (3)$$

$$q\Delta N_{st} = C_{ox}\Delta V_{hys} \quad (4)$$

where, the accumulation capacitance equivalent thickness (CET) = $3.9\epsilon_0/C_{ox}$, V_{min} is the starting voltage, ϵ_0 is the absolute permittivity in the free space, and ΔV_{hys} is the change in hysteresis voltage. The hysteresis was measured at 1 MHz[9,70,78] for both devices by varying V_{start} from 2 to 1 V in steps of 0.1 V, while V_{stop} remained. Lowering the V_{start} value decreases the magnitude of the hysteresis, as shown in Figure 4c,d. With the measured ΔV_{hys} and calculated E_{ox}, N_{st} values were calculated for the w/ACM vIL and w/o IL, as shown in Figure 4e. The N_{st} of the w/ACM vIL and w/o IL ranged from 10^{10} and 10^{12} cm^{-2} in the E_{ox} range from 80 to 220 MV cm^{-1}, respectively. The N_{st} of the w/ACM vIL is 2 orders of magnitude lower than that of the w/o IL across all applied E_{ox} regions, suggesting that ACM vIL minimizes the oxide trap density. The improved oxide quality was further supported by leakage current characteristics. Figure 4f illustrates the leakage current density characteristics ($J-V$) with an applied bias of −2 to +2 V. The measured off-state leakage current density was reduced by 1 order of magnitude in the w/ACM vIL, measuring 6.65×10^{-7} A cm^{-2}, compared to the w/o IL, which measured 2.44×10^{-6} A cm^{-2}. Furthermore, to investigate the thermal stability and evaluate the role of the ACM vIL in the dynamics of charge carriers, we performed temperature-dependent $J-V$ measurements for w/o IL and ACM vIL, and the results are presented in Figure S8 (a detailed explanation is provided in Supporting Information). Additionally, the voltage-dependent capacitance−frequency characteristics ($C-F$) were measured to find C_{ox} and dielectric permittivity for the w/o IL and w/ACM vIL devices (Figure 4g,h). The dielectric permittivity of w/o IL and w/ACM vIL were determined to be 6.87 and 7.33, respectively, from the measured $C-F$ data. The MOS electrical device parameters are tabulated in Figure 3h. The comprehensive analysis of the $C-V$, $G-V$, N_{st}, and $J-V$ decisively demonstrates that ACM vIL

https://doi.org/10.1021/acsnano.4c12780
ACS Nano 2025, 19, 1056−1069

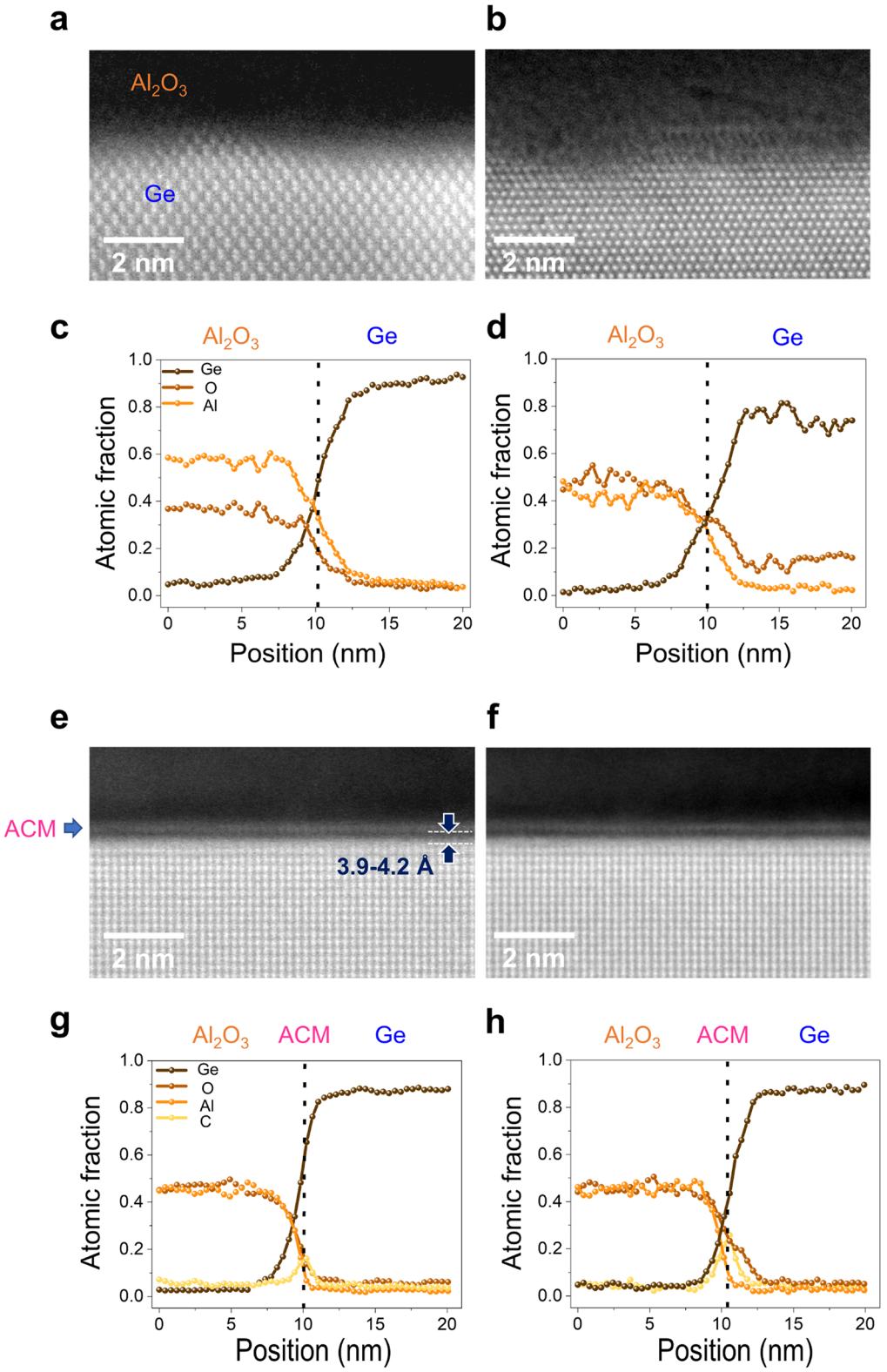

Figure 5. STEM analysis to determine the role of ACM as a passivation layer and diffusion barrier. Cross-sectional ADF−STEM images of the (a) As-fabricated, and (b) Post annealed at 500 °C of the w/o IL, exhibiting the interface roughness and diffusion between Al_2O_3 and Ge. (e) and (f) Corresponding images of the w/ACM vIL, highlighting the flat and preserved sharp interface, even after annealing at 500 °C for 6 h. The ACM vILs are distinctly visible at the Al_2O_3 and H−Ge interface. Hydrogen termination of Ge is not directly observable owing to the contrast in atomic numbers. However, the interatomic distance between the ACM and the topmost Ge atom is measured as 3.9−4.2 Å. (c), (d), (g) and (h) EDS line profiles of the respective MOSCAPs. The line profiles for the w/o IL ((c) and (d)) show notable interdiffusion, made evident by the atomic fractions of the Al and Ge across the interface. For the w/ACM vIL ((g) and (h)) a pronounced carbon peak (pale yellow) at the interface indicates its presence, while the decreased atomic fractions of the Al and Ge reflect the efficiency of ACM as a diffusion barrier, enhancing the reliability of the MOSCAP.

https://doi.org/10.1021/acsnano.4c12780
ACS Nano 2025, 19, 1056−1069

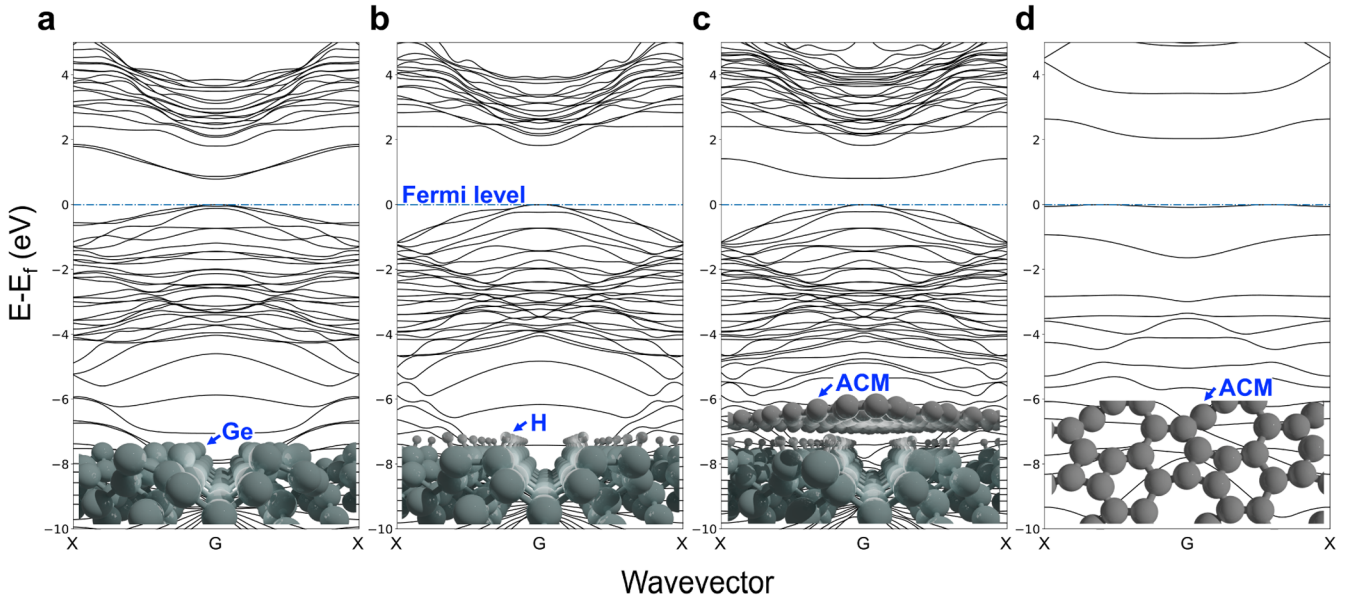

Figure 6. Effect of ACM on the electronic band structure of the H−Ge. (a) Band structure of the Ge(100) with the a(2 × 1) reconstruction, showing a small bandgap at the γ point. (b) The H−Ge(100) system showing the disappearance of gap states upon the unbuckling of the surface Ge dimer, resulting in a wider bandgap, compared to the buckled Ge(100) system. (c) The ACM/H−Ge(100) system indicating a distinct state within the bandgap, different from Ge buckling. (d) Illustration of the ACM structure, consisting of penta-, hexa-, and octa-carbon rings. The visualization at the bottom of each graph depicts the respective atomic configuration. The dashed line with sky blue color represented the top of the valence band.

considerably enhances the interface quality between Al_2O_3 and H−Ge and improves the quality of the oxide on the ACM/H−Ge surface.

ACM as an Effective One-Atom-Thick Diffusion Barrier: STEM Analysis. To investigate the role of ACM as a passivation layer for the H−Ge surface and a diffusion barrier between the gate oxide and the semiconductor, STEM was employed. The w/o IL and w/ACM vIL were annealed at 500 °C in an Ar atmosphere for 6 h to evaluate the function of the diffusion barrier. Figure 5a,b,e,f show cross-sectional annular dark-field (ADF) STEM images of the as-fabricated and annealed w/o IL (Figure 5a,b), and w/ACM vIL (Figure 5e,f), respectively. A distinct carbon monolayer is observable at the interface between Al_2O_3 and the H−Ge substrate, sustaining a highly flat interface, regardless of the 500 °C annealing (Figure 5e,f). Hydrogen termination on the Ge surface was not detectable in the ADF−STEM images owing to the low atomic number of hydrogen, as the atomic number mainly dominates the image contrast. Nevertheless, our DFT calculation confirms that the thermodynamically stable interatomic distance between the ACM and the topmost H−Ge atom (~4 Å) corresponds to the measured interatomic distance between the ACM and the topmost H−Ge atom of (3.9−4.2 Å). This indirectly confirms that the ACM serves as a passivation layer for the H-terminated Ge. In contrast to the w/ACM vIL shown in Figure 5e,f, the interface between the Al_2O_3 and the Ge substrate in the w/o IL (Figure 5a,b) exhibits poor quality, showing severe roughness of the Ge substrate toward the Al_2O_3 in both the as-fabricated MOSCAP and the annealed MOSCAP, which substantially degrades the performance of the MOSCAP.

In addition to the atomic resolution ADF−STEM images, the energy dispersive X-ray spectroscopy (EDS) line profiles from Al_2O_3 to the H−Ge substrate reveal that ACM serves as an effective diffusion barrier. Figure 5c,d,g,h show the EDS line profiles of the MOSCAPs, acquired from the same cross-sectional specimen as shown in Figure 5a,b,e,f, respectively. The line profiles of the w/o ACM shown in Figure 5c,d, reveal relatively high atomic fractions of Al (orange) and Ge (reddish-brown) across the interface, indicated by a black dotted line. This means interdiffusion occurs during both MOSCAP fabrication and heat treatment steps. In contrast, in the line profiles of the w/ACM vIL shown in Figure 5g,h, a sharp increase in the atomic fraction of carbon appears at the interface, corresponding to the location of the ACM in the ADF−STEM images. Compared to Figure 5a,b, the interdiffusion between Al_2O_3 and the H−Ge substrate is suppressed, showing relatively low atomic fractions of Al and H−Ge across the ACM interface. The STEM and EDS results confirm that ACM acts as an excellent diffusion barrier and creates a vdW interface on the H−Ge surface, eventually ensuring the reliability of the MOSCAP. To validate the thermal stability of the ACM vIL, we evaluated the electrical performance of both w/o IL and w/ACM vIL following annealing at 500 °C for 6 h, as shown in Figure S9. The results indicate that the w/ACM vIL retained its performance postannealing, confirming that the ACM vIL provides excellent thermal stability, essential for maintaining device reliability during high-temperature processing.

Effect of ACM vIL on the Electronic Band Structure of the H−Ge Surface: DFT Calculations. Utilizing DFT calculations, we developed band structures for Ge(100) with various terminations to validate our experimental findings. The computational methodology involved preparing a mirrored Ge(100) slab to ensure the accuracy of the band structure through a hybrid functional approach. Similar to surface reconstructions observed in Si(100), the Ge(100) surface atoms exhibited Ge−Ge buckling or dimerization tendencies. While p(2 × 1) or c(4 × 2) reconstructions generally exhibited greater stability than asymmetric ones (referred to as a(2 ×

https://doi.org/10.1021/acsnano.4c12780
ACS Nano 2025, 19, 1056−1069

1)),[79] we opted for a(2 × 1) owing to the substantial computational resources required for precise band structure calculations using the PBE0 hybrid functional. Detailed explanations about structural modeling and input parameters for calculation were denoted in Figure S12. In the H−Ge(100) system, strategic placement of H atoms on the entire buckled Ge atoms aimed to unbuckle them. Shifting focus to ACM modeling, we used high-temperature molecular dynamics and quenching to develop a random structure corresponding to an ACM with penta, hexa, and octa-carbon rings. This randomly generated structure is believed to capture the amorphous nature of ACM, emphasized using the opened bandgap in Figure 6d. Subsequently, the ACM was attached to the top of the H−Ge(100) slab, forming the ACM/H−Ge(100) system.

As shown in Figure 6, we developed band structures for each system discussed in the preceding paragraph. The Ge(100) surface, characterized by the a(2 × 1) reconstruction, exhibited a small bandgap at the γ point (Figure 6a). Upon unbuckling the surface Ge dimer, we observed the disappearance of gap states, while other states remained unaffected (Figure 6b), resulting in a broader bandgap, compared to the buckled Ge(100) system. This observation precisely corroborates our experimental findings. Essentially, we can assert that Ge−Ge buckling on the surface considerably contributes to the high conductivity of gap states. In the case of the ACM/H−Ge(100), a new state within the bandgap is also observed (Figure 6c), distinct from the effects of Ge buckling. While surface reconstruction on Ge(100) would uniformly occur across the entire surface, the generation of the gap state via ACM was entirely contingent on the local structure. Consequently, electrons in the gap state exhibit localization, providing no discernible benefit to the conductivity of the system. The DFT study confirms that ACM vdW bonding on the H−Ge(100) surface does not alter the electronic band structure of the H−Ge(100) based on Figure 6b,c, suggesting that ACM can be utilized as an effective IL in a MOSCAP.

CONCLUSIONS

We report the potential of one-atom-thick ACM as a vIL in addressing the critical challenges of interface and oxide quality in the Al_2O_3/H−Ge MOSCAPs, contributing to the downscaling of semiconductor devices. Direct synthesis of ACM on the H−Ge surface revealed superior passivation and the H−Ge surface was preserved without inducing surface reconstruction. By utilizing the advantages of the ACM, such as impermeability, vdW bonding on other material surfaces, insulating characteristics, and its function as a seeding layer, we observed a significant improvement in the interfacial properties with a $D_{it,max}$ of 7.21 × 10^{10} cm^{-2} eV^{-1}, compiles with the ITRS recommendations for ultrasmall-scale devices. Other key parameters, including the $C-V$ hysteresis width, N_{st}, and leakage currents, are reduced in the w/ACM vIL, demonstrating the enhanced quality of the Al_2O_3 on the ACM without interdiffusion. Furthermore, DFT calculations clarify that ACM does not alter the electronic band structure of H−Ge(100), suggesting the ACM as an effective IL. Additionally, cross-sectional ADF-STEM images of 5 nm thick Al_2O_3 with the ACM vIL (Figure S10) showed a sharp and well-defined interface, confirming the preservation of interface integrity at reduced oxide thicknesses. Moreover, devices incorporating a 5 nm thick high-k dielectric HfO_2 with the ACM vIL (Figure S11) exhibited similar improved performance as the 20 nm thick Al_2O_3 with the ACM vIL. These results suggest that the ACM vIL works effectively for ultrasmall-scale devices and is compatible with other high-k dielectrics. Nobel laureate Herbert Kroemer stated that "the interface is the device".[80] Indeed, the ACM vIL acts as a multifunctional device component in the high-k/H−Ge MOSCAP. Our approach using ACM vIL proposes a pathway to improve device properties at ultrasmall-scale.

METHODS

Synthesis of the ACM on the H−Ge Surface. The ACM was synthesized on Ga-doped p-type Ge(100) substrates with a resistivity of 0.5−1.0 Ω cm using a customized LP−CVD system operating at 850 to 700 °C. Before synthesis, the substrates were cleaned via sonication in acetone, isopropyl alcohol, and deionized water to remove organic residues. Next, the native oxide was removed by immersing the substrates in a 2% hydrogen fluoride solution, and then dried them in the air using an N_2 blower. These H-terminated substrates were loaded into the LP−CVD chamber, which was then evacuated to 6 × 10^{-6} Torr, and heated to the desired deposition temperature. The growth rate of the ACM was increased by stabilizing the chamber environment with H_2 gas for 15 min. ACM was then synthesized using a mixture of CH_4 and H_2 gas (ultrahigh purity grade, 99.999%) at a working pressure of 20 Torr for 30 min. Finally, the CH_4 supply was turned off, and the chamber was rapidly cooled to 40 °C in the presence of H_2 gas to prevent the crystallization of the H−Ge surface.

Fabrication of the MOSCAP. The Al_2O_3 dielectric layer was deposited on both ACM/H−Ge and Ge wafers using a thermal atomic layer deposition (ALD) reactor (CN1 Co.). After cleaning the Ge substrates, the samples were transferred to the ALD reactor. Initially, the chamber was evacuated to a pressure of 7.6 × 10^{-3} Torr, and trimethyl aluminum (TMA) and H_2O were used as precursors and reactants for Al_2O_3 depositions. Before the reaction, pretreatment passivation was performed using H_2 gas to suppress the surface states of the Ge substrate. The doses of TMA, Ar, and H_2O were applied for 0.1, 15, and 0.1 s, respectively, in the reactor at 150 °C for Al_2O_3 deposition. To fabricate the MOSCAP structure, a 100 nm thick Al layer was deposited via thermal evaporation to form circular gates with a diameter of 300 μm, and a bottom contact was deposited with 10 nm thick Ti and 100 nm thick Al layers. Finally, postdeposition annealing was performed in a tubular furnace at 350 °C for 30 min in an Ar atmosphere.

Plan-View HR-TEM. To analyze the microstructure of both graphene and ACM, we employed an Au-assisted transfer method to transfer them onto a perforated silicon nitride TEM grid. Initially, a 30 nm thick gold film was deposited onto the surface of the ACM grown on the H−Ge substrate using e-beam evaporation (WOOSUNG Hi-vac). Subsequently, the Au-coated specimen was gently floated onto a mixture of hydrofluoric acid and hydrogen peroxide to detach the Au/ACM film from the H−Ge substrate. The film was then rinsed by floating it on DI water more than three times. Next, we scooped the film onto a grid with a hole diameter of 1 μm and dried it in a 70 °C dry oven for 6 h. Finally, the fabricated grid was immersed in a gold etchant (Sigma-Aldrich) to remove the Au film, and it was rinsed in DI water several times. The prepared graphene and ACM were analyzed using an aberration-corrected ThermoFisher Titan cubed G2 60−300 operating at 80 kV, equipped with a monochromator. The microscope provides sub angstrom resolution at 80 kV and ∼ −13 μm of spherical aberration. The typical electron beam densities were adjusted to ∼5 × 10^5 e^- nm^{-2}. Atomic images were obtained using a white atom contrast to capture the actual atom positions under properly focused conditions, which is essential for direct image interpretation.

Cross-Sectional TEM Sample Preparation and STEM/EDS Analysis. To acquire a cross-sectional view of the sample, we prepared a STEM specimen utilizing a focused ion beam (ThermoFisher Helios 450HP FIB). Initially, a carbon protection layer was applied to the surface of the MOSCAPs to preserve their microstructure from ion milling. Subsequently, we employed a Ga

https://doi.org/10.1021/acsnano.4c12780
ACS Nano 2025, 19, 1056−1069

ion beam with 30 kV accelerating voltage and 2.1 nA beam current to etch the remaining area and create a cross-sectional lamella. The lamella was then carefully lifted out from the MOSCAPs, and affixed to the side wall of the TEM half grid post, to mitigate potential contamination from the FIB grid. To render the lamella electron beam transparent, we further thinned it to <100 nm. Finally, a Ga ion beam of 5 kV accelerating voltage with 44 pA current was applied to polish the damaged layers on the lamella. The ADF−STEM images were obtained using an aberration-corrected ThermoFisher Titan cubed G2 60−300 operating at 200 kV, with a convergence angle of 26.6 mrad and probe current of ∼60 pA. The ADF−STEM images were generated by stacking a series of seven single-scanned images using the drift-corrected frame imaging function in Velox software (ThermoFisher). For acquiring an elemental line profile along the metal/oxide/semiconductor structure, the Super-X system of the TEM was utilized, and EDS line profile data were obtained by integrating the signal of the STEM−EDS images using Velox software.

Raman Spectroscopy. The ACM samples grown on H−Ge substrates were transferred to SiO_2 (300 nm)/Si substrates using an Au-assisted transfer method, as detailed in the plan-view HR−TEM section, to characterize the microstructure of the ACM through Raman spectroscopy (WITec alpha300 R), which was equipped with a 532 nm laser. Raman spectra were appropriately calibrated with reference to the 520 cm^{-1} peak of Si. The laser power was adjusted to ∼0.8 mW to prevent potential damage to the ACM, and the exposure time was set to 1 min to ensure an adequate response.

Electrical Property Characterization. Electrical measurements were conducted in ambient conditions in a dark shield probe station (MS TECH Co.). *C*−*V* and *C*−*F* measurements were carried out using a precision LCR meter (Keysight E4980A, 20 Hz−5 MHz). The *G*−*V* measurements in parallel mode utilized a dedicated DC source unit within the precision LCR meter. The *J*−*V* characteristics were determined using a semiconductor parameter analyzer (HP4155B).

Computational Details. The plane-wave based DFT calculations in this research were performed using the Vienna *ab initio* simulation package.[81] The generalized gradient approximation level of the Perdew−Burke−Ernzerhof (PBE) exchange−correlation functional[82,83] was used for geometry optimization. To determine the accurate band structure, the PBE0 hybrid functional[84,85] was employed. A cutoff energy of 400 eV was utilized, and the Brillouin zone was sampled at 5 × 5 × 1 based on the *γ*-centered scheme. Convergence criteria for electronic and geometric optimizations were set to 10^{-6} eV and 10^{-2} eVÅ^{-1}, respectively. The Ge(001) slab model, identical to our experimental setup, was developed with the middle layer mirrored along the *z*-direction to ensure identical termination of both the top and bottom layers. The middle five layers were fixed in their bulk position among the 13 atomic layers, and the entire slab was centered within a 20 Å vacuum gap, as shown in Figure S12. We also prepared H-terminated Ge(001) slab (noted as H/Ge(001)) and the ACM with the H-terminated Ge(001) slab (recorded as ACM/H/Ge(001)) to compare band structure changes.

ASSOCIATED CONTENT

Supporting Information

The Supporting Information is available free of charge at https://pubs.acs.org/doi/10.1021/acsnano.4c12780.

Wetting and dewetting of Al_2O_3 on SCG/Ge and ACM/H−Ge, sheet resistance characterization of G-FETs, *I*−*V* measurements of the ACM-FET, TCAD simulations of the impact of the 80 MΩ/square sheet resistance of ACM vIL on a Ge-MOSFET, Raman mapping of ACM at various synthesis temperatures, fwhm(G) Raman map of the ACM sample, HR-TEM images of SCG, NCG, and ACM structures, Temperature dependence leakage current density, Electrical characteristics of the MOS-CAP before and after 500 °C annealing, ADF-STEM images for thin dielectrics, Electrical performance of 5 nm thick HfO_2 MOSCAP, surface variations of Ge(100), series resistance correction analysis, capacitance calculations, and a comparison of passivation methods in Ge/high-*k* MOS structures (PDF)

AUTHOR INFORMATION

Corresponding Authors

Sangyeob Lee − *Department of Materials Science and Engineering, Hanbat National University, Daejeon 34158, Republic of Korea;* orcid.org/0000-0002-9957-990X; Email: sangyeob@hanbat.ac.kr

Zonghoon Lee − *Center for Multidimensional Carbon Materials, Institute for Basic Science and Department of Materials Science and Engineering, Ulsan National Institute of Science and Technology, Ulsan 44919, Republic of Korea;* orcid.org/0000-0003-3246-4072; Email: zhlee@unist.ac.kr

Jae-Hyun Lee − *Department of Energy System Research and Department of Materials Science and Engineering, Ajou University, Suwon 16499, Republic of Korea; Institute for Functional Intelligent Materials, National University of Singapore, Singapore 117575, Singapore; Department of Electrical and Computer Engineering, Sungkyunkwan University, Suwon 16419, Republic of Korea;* orcid.org/0000-0001-5117-8923; Email: jaehyunlee@ajou.ac.kr

Choong-Heui Chung − *Department of Materials Science and Engineering, Hanbat National University, Daejeon 34158, Republic of Korea;* orcid.org/0000-0003-1947-732X; Email: choong@hanbat.ac.kr

Authors

Viswanath G. Akkili − *Department of Materials Science and Engineering, Hanbat National University, Daejeon 34158, Republic of Korea;* orcid.org/0000-0001-9232-4536

Jongchan Yoon − *Center for Multidimensional Carbon Materials, Institute for Basic Science and Department of Materials Science and Engineering, Ulsan National Institute of Science and Technology, Ulsan 44919, Republic of Korea*

Kihyun Shin − *Department of Materials Science and Engineering, Hanbat National University, Daejeon 34158, Republic of Korea*

Sanghyun Jeong − *Department of Materials Science and Engineering, Hanbat National University, Daejeon 34158, Republic of Korea;* orcid.org/0009-0007-4178-0524

Ji-Yun Moon − *Mechanical Engineering and Materials Science, Washington University, St. Louis, Missouri 63130, United States*

Jun-Hui Choi − *Department of Energy System Research and Department of Materials Science and Engineering, Ajou University, Suwon 16499, Republic of Korea*

Seung-Il Kim − *Mechanical Engineering and Materials Science, Washington University, St. Louis, Missouri 63130, United States; Department of Energy System Research and Department of Materials Science and Engineering, Ajou University, Suwon 16499, Republic of Korea*

Ashish A. Patil − *Department of Materials Science and Engineering, Hanbat National University, Daejeon 34158, Republic of Korea;* orcid.org/0000-0003-2612-6915

Frederick Aziadzo − *Department of Materials Science and Engineering, Hanbat National University, Daejeon 34158, Republic of Korea;* orcid.org/0000-0002-1741-8986

Jeongbeen Kim − *Department of Materials Science and Engineering, Hanbat National University, Daejeon 34158, Republic of Korea*

https://doi.org/10.1021/acsnano.4c12780
ACS Nano 2025, 19, 1056−1069

Suhyeon Kim − *Department of Materials Science and Engineering, Hanbat National University, Daejeon 34158, Republic of Korea;* orcid.org/0009-0007-2822-227X
Dong-Wook Shin − *Department of Materials Science and Engineering, Hanbat National University, Daejeon 34158, Republic of Korea*
Jung-Sub Wi − *Department of Materials Science and Engineering, Hanbat National University, Daejeon 34158, Republic of Korea;* orcid.org/0000-0002-9531-2001
Hoon-Hwe Cho − *Department of Materials Science and Engineering, Hanbat National University, Daejeon 34158, Republic of Korea;* orcid.org/0000-0002-9815-3739
Joon Sik Park − *Department of Materials Science and Engineering, Hanbat National University, Daejeon 34158, Republic of Korea;* orcid.org/0000-0003-1080-7863
Eui-Tae Kim − *Department of Materials Science and Engineering, Chungnam National University, Daejeon 34134, Republic of Korea;* orcid.org/0000-0002-5488-7159
Dong-Eun Kim − *National Institute for Nanomaterials Technology, Pohang University of Science and Technology, Pohang 37673, Republic of Korea*
Jaeyeong Heo − *Department of Materials Science and Engineering, Chonnam National University, Gwangju 61186, Republic of Korea;* orcid.org/0000-0002-2602-6538
Graeme Henkelman − *Department of Chemistry and the Oden Institute for Computational Engineering and Science, The University of Texas, Austin, Texas 78712-1224, United States;* orcid.org/0000-0002-0336-7153
Kostya S. Novoselov − *Institute for Functional Intelligent Materials, National University of Singapore, Singapore 117575, Singapore*

Complete contact information is available at: https://pubs.acs.org/10.1021/acsnano.4c12780

Author Contributions

[¶]V.G.A., J.Y., and K.S. contributed equally. S.L. and C.H.C. conceived the idea for this research and supervised the project. V.G.A. designed and performed the electrical measurements and analyzed the data. J.Y. and Z.L. carried out TEM measurements and performed the structural analysis. J.Y.M., J.H.C., S.I.K., and J.H.L. designed the ACM synthetic method and carried out the Raman analysis. K.S. and G.H. developed the theoretical models and performed the DFT calculations. S.J., D.E.K., A.A.P., F.A., J.K., and S.K. fabricated the MOSCAP device and conducted electrical characterization. V.G.A., J.Y., K.S., and J.Y.M. wrote the manuscript with input from D.W.S., J.S.W., H.H.C., J.S.P., E.T.K., J.H., and K.S.N. All the authors discussed the data and manuscript.

Notes

The authors declare no competing financial interest.

ACKNOWLEDGMENTS

This work was supported by the National Research Foundation of Korea (grant no. 2021R1I1A3047372, 2021RIS-004) and the Institute for Basic Science (grant no. IBS-R019-G1).

REFERENCES

(1) IEEE International Roadmap for Devices and Systems-More Moore, 2023, https://irds.ieee.org/images/files/pdf/2023/2023IRDS_MM.pdf (accessed 2023)
(2) Li, W.; Zhou, J.; Cai, S.; Yu, Z.; Zhang, J.; Fang, N.; Li, T.; Wu, Y.; Chen, T.; Xie, X.; et al. Uniform and ultrathin high-κ gate dielectrics for two-dimensional electronic devices. *Nat. Elect.* **2019**, *2*, 563−571.
(3) Heiman, F. P.; Warfield, G. The Effects of Oxide Traps on the MOS Capacitance. *IEEE Trans. Electron Devices* **1965**, *12*, 167−178.
(4) Sun, X.; Merckling, C.; Brammertz, G.; Lin, D.; Dekoster, J.; Cui, S.; Ma, T. P. Improved AC conductance and Gray-Brown methods to characterize fast and slow traps in Ge metal−oxide−semiconductor capacitors. *J. Appl. Phys.* **2012**, *111*, No. 054102.
(5) Taoka, N.; Mizubayashi, W.; Morita, Y.; Migita, S.; Ota, H.; Takagi, S. Nature of interface traps in Ge metal-insulator-semiconductor structures with GeO_2 interfacial layers. *J. Appl. Phys.* **2011**, *109*, No. 084508.
(6) Sze, S. M.; Ng, K. K. *Physics of Semiconductor Devices*, 3rd ed.; *rd ed*Wiley-Interscience: Hoboken, NJ, 2007; pp 1−832.
(7) Sze, S. M.; Lee, M.-K. *Semiconductor Devices: Physics and Technology*, 3rd ed.; Wiley: Hoboken, NJ, 2012; pp 1−592.
(8) Ke, M.; Yu, X.; Chang, C.; Takenaka, M.; Takagi, S. Properties of slow traps of ALD Al_2O_3/GeO_x/Ge nMOSFETs with plasma post oxidation. *Appl. Phys. Lett.* **2016**, *109*, No. 032101.
(9) Ke, M.; Takenaka, M.; Takagi, S. Slow Trap Properties and Generation in Al_2O_3/GeO_x/Ge MOS Interfaces Formed by Plasma Oxidation Process. *ACS Appl. Electron. Mater.* **2019**, *1*, 311−317.
(10) Jiang, S.; He, G.; Liu, M.; Zhu, L.; Liang, S.; Li, W.; Sun, Z.; Tian, M. Interface Modulation and Optimization of Electrical Properties of HfGdO/GaAs Gate Stacks by ALD-Derived Al_2O_3 Passivation Layer and Forming Gas Annealing. *Adv. Electron. Mater.* **2018**, *4*, No. 1700543.
(11) Kim, D. G.; An, C. H.; Kim, S. H.; Kwon, D. S.; Lim, J.; Jeon, W.; Hwang, C. S. Optimized Al-doped TiO_2 gate insulator for a metal-oxide-semiconductor capacitor on a Ge substrate. *J. Mater. Chem. C* **2021**, *9*, 1572−1583.
(12) Kim, D.-O.; Hong, H.-K.; Seo, D.-B.; Trung, T. N.; Hwang, C.-C.; Lee, Z.; Kim, E.-T. Novel high-*k* gate dielectric properties of ultrathin hydrocarbon films for next-generation metal-insulator-semiconductor devices. *Carbon* **2020**, *158*, 513−518.
(13) Gaddam, V.; Das, D.; Jeon, S. Insertion of HfO_2 Seed/Dielectric Layer to the Ferroelectric HZO Films for Heightened Remanent Polarization in MFM Capacitors. *IEEE Trans. Electron Devices* **2020**, *67*, 745−750.
(14) Cheema, S. S.; Shanker, N.; Wang, L. C.; Hsu, C. H.; Hsu, S. L.; Liao, Y. H.; San Jose, M.; Gomez, J.; Chakraborty, W.; Li, W. S.; et al. Ultrathin ferroic HfO_2-ZrO_2 superlattice gate stack for advanced transistors. *Nature* **2022**, *604*, 65−71.
(15) Jo, S.; Lee, H. Y. S.; Choe, D. H.; Kim, J. H.; Lee, Y. S.; Kwon, O.; Nam, S.; Park, Y.; Kim, K.; Chae, B. G.; et al. Negative differential capacitance in ultrathin ferroelectric hafnia. *Nat. Elect.* **2023**, *6*, 390−397.
(16) Chen, K.-H.; Lin, C.-Y.; Chen, M.-C.; Lin, Y.-S.; Chang, Y.-C.; Lin, Y.-H.; Jin, F.-Y.; Ciou, F.-M.; Chang, K.-C.; Hung, W.-C.; et al. Advanced Low-Temperature−High-Pressure Hydrogen Treatment for Interface Defect Passivation in Si- and SiGe-Channel MOSCAPs. *IEEE Trans. Electron Devices* **2020**, *67*, 5403−5407.
(17) Choi, K.-K.; Kee, J.; Park, C.-G.; Kim, D.-k. Effects of H_2 plasma and annealing on atomic-layer-deposited Al_2O_3 films and Al/Al_2O_3/Si structures. *Appl. Phys. Express* **2015**, *8*, 045801 DOI: 10.7567/apex.8.045801.
(18) Kobayashi, H.; Imamura, K.; Fukayama, K.-i.; Im, S.-S.; Maida, O.; Kim, Y.-B.; Kim, H.-C.; Choi, D.-K. Complete prevention of reaction at HfO_2/Si interfaces by 1nm silicon nitride layer. *Surf. Sci.* **2008**, *602*, 1948−1953.
(19) Paskaleva, A.; Spassov, D.; Atanassova, E. Impact of Si substrate nitridation on electrical characteristics of Ta_2O_5 stack capacitors. *J. Phys. D: Appl. Phys.* **2007**, *40*, 6709−6717.
(20) Kavrik, M. S.; Ercius, P.; Cheung, J.; Tang, K.; Wang, Q.; Fruhberger, B.; Kim, M.; Taur, Y.; McIntyre, P. C.; Kummel, A. C. Engineering High-*k*/SiGe Interface with ALD Oxide for Selective GeO_x Reduction. *ACS Appl. Mater. Interfaces* **2019**, *11*, 15111−15121.

(21) Mallem, K.; Jagadeesh Chandra, S. V.; Ju, M.; Dutta, S.; Phanchanan, S.; Sanyal, S.; Pham, D. P.; Hussain, S. Q.; Kim, Y.; Park, J.; et al. Effects of post deposition annealing atmosphere on interfacial and electrical properties of HfO_2/Ge_3N_4 gate stacks. *Thin Solid Films* **2019**, *675*, 16−22.
(22) Contreras-Guerrero, R.; Edirisooriya, M.; Noriega, O. C.; Droopad, R. Interface properties of MBE grown epitaxial oxides on GaAs. *J. Cryst. Growth* **2013**, *378*, 238−242.
(23) Zhang, R.; Iwasaki, T.; Taoka, N.; Takenaka, M.; Takagi, S. Al_2O_3/GeO_x/Ge gate stacks with low interface trap density fabricated by electron cyclotron resonance plasma postoxidation. *Appl. Phys. Lett.* **2011**, *98*, No. 112902.
(24) Delabie, A.; Bellenger, F.; Houssa, M.; Conard, T.; Van Elshocht, S.; Caymax, M.; Heyns, M.; Meuris, M. Effective electrical passivation of Ge(100) for high-*k* gate dielectric layers using germanium oxide. *Appl. Phys. Lett.* **2007**, *91*, No. 082904.
(25) Pascu, R.; Romanitan, C.; Varasteanu, P.; Kusko, M. A Reliable Technology for Advanced SiC-MOS Devices Based on Fabrication of High Quality Silicon Oxide Layers by Converting a-Si. *IEEE J. Electron Devices Soc.* **2019**, *7*, 158−167.
(26) Fukuda, Y.; Yazaki, Y.; Otani, Y.; Sato, T.; Toyota, H.; Ono, T. Low-Temperature Formation of High-Quality GeO_2 Interlayer for High-*k* Gate Dielectrics/Ge by Electron-Cyclotron-Resonance Plasma Techniques. *IEEE Trans. Electron Devices* **2010**, *57*, 282−287.
(27) Joo, W. J.; Lee, J. H.; Jang, Y.; Kang, S. G.; Kwon, Y. N.; Chung, J.; Lee, S.; Kim, C.; Kim, T. H.; Yang, C. W.; et al. Realization of continuous Zachariasen carbon monolayer. *Sci. Adv.* **2017**, *3*, No. e1601821.
(28) Tian, H.; Ma, Y.; Li, Z.; Cheng, M.; Ning, S.; Han, E.; Xu, M.; Zhang, P. F.; Zhao, K.; Li, R.; et al. Disorder-tuned conductivity in amorphous monolayer carbon. *Nature* **2023**, *615*, 56−61.
(29) Allen, K. D.; Wegener, G.; Matthew Sublett, D., Jr.; Bodnar, R. J.; Feng, X.; Wendt, J.; White, R. H. Biogenic formation of amorphous carbon by anaerobic methanotrophs and select methanogens. *Sci. Adv.* **2021**, *7*, No. eabg9739.
(30) Bunch, J. S.; Verbridge, S. S.; Alden, J. S.; van der Zande, A. M.; Parpia, J. M.; Craighead, H. G.; McEuen, P. L. Impermeable Atomic Membranes from Graphene Sheets. *Nano Lett.* **2008**, *8*, 2458−2462.
(31) Geim, A. K. Graphene: Status and Prospects. *Science* **2009**, *324*, 1530−1534.
(32) Rivillon, S.; Chabal, Y. J.; Amy, F.; Kahn, A. Hydrogen passivation of germanium (100) surface using wet chemical preparation. *Appl. Phys. Lett.* **2005**, *87*, No. 253101.
(33) Sioncke, S.; Chaba, Y. J.; Frank, M. M. Germanium Surface Conditioning and Passivation. In *Handbook of Cleaning in Semiconductor Manufacturing: Fundamental and Applications*; Wiley: Hoboken, NJ, 2010; pp 429−472.
(34) Barrigón, E.; Brückner, S.; Supplie, O.; Kleinschmidt, P.; Rey-Stolle, I.; Hannappel, T. Optical in situ monitoring of hydrogen desorption from Ge(100) surfaces. *Appl. Phys. Lett.* **2013**, *102*, No. 111608.
(35) Tsoi, S.; Pratibha, D.; Adam, L. F.; Rory, S.; Jeremy, T. R.; Thomas, L. R.; Paul, E. S. van der Waals Screening by Single-Layer Graphene and Molybdenum Disulfide. *ACS Nano* **2014**, *8*, 12410−12417.
(36) Moser, J.; Tao, H.; Roche, S.; Alzina, F.; Sotomayor Torres, C. M.; Bachtold, A. Magnetotransport in disordered graphene exposed to ozone: From weak to strong localization. *Phys. Rev. B* **2010**, *81*, No. 205445.
(37) Van Tuan, D.; Kumar, A.; Roche, S.; Ortmann, F.; Thorpe, M. F.; Ordejon, P. Insulating behavior of an amorphous graphene membrane. *Phys. Rev. B* **2012**, *86*, No. 121408.
(38) Zhao, L.; Bardel, D.; Maynadier, A.; Nelias, D. Velocity correlated crack front and surface marks in single crystalline silicon. *Nat. Commun.* **2018**, *9*, No. 1298.
(39) Lee, J. S.; Kaufman-Osborn, T.; Melitz, W.; Lee, S.; Kummel, A. Effect of H_2O chemisorption on passivation of Ge(100) surface studied by scanning tunneling microscopy. *Surf. Sci.* **2011**, *605*, 1583−1588.
(40) Lee, S. Surface potential measurements of 2 × 1 reconstructed Si(001) using UHV Kelvin probe force microscopy. *Surf. Sci.* **2015**, *641*, 16−22.
(41) Ozasa, K.; Ito, H.; Maeda, M.; Hara, M. Surface-potential undulation of Alq3 thin films prepared on ITO, Au, and n-Si. *J. Nanosci. Nanotechnol.* **2012**, *12*, 499−502.
(42) Ozasa, K.; Ito, H.; Maeda, M.; Hara, M. Photoinduced evolution of surface-potential undulation observed on vacuum-deposited thin films of tris(8-hydroxyquinolinato) aluminum. *Appl. Phys. Lett.* **2011**, *98*, No. 013301.
(43) Sze, S. M.; Irvin, J. C. Resistivity, mobility and impurity levels in GaAs, Ge, and Si at 300 K. *Solid·State Electron.* **1968**, *11*, 599−602.
(44) Prabhakaran, K.; Ogino, T. Oxidation of Ge(100) and Ge(111) surfaces: an UPS and XPS study. *Surf. Sci.* **1995**, *325*, 263−271.
(45) Hwang, J.; Changshin, J.; Min Gyu, K.; Jinyoung, C.; Eunho, L.; Seongseop, K.; Sanha, J.; Youngsik, K.; Jinwoo, L. Mesoporous Ge/GeO_2/Carbon Lithium-Ion Battery Anodes with High Capacity and High Reversibility. *ACS Nano* **2015**, *9*, 5299−5309.
(46) *Bias Temperature Instability for Devices and Circuits*; Grasser, T., Ed.; Springer: New York, 2014; pp 1−783.
(47) Lee, J. S.; Bishop, S. R.; Kaufman-Osborn, T.; Chagarov, E.; Kummel, A. C. Monolayer Passivation of Ge(100) Surface via Nitridation and Oxidation. *ECST* **2010**, *33*, 447−454.
(48) Wojtaszek, M.; Zuzak, R.; Godlewski, S.; Kolmer, M.; Lis, J.; Such, B.; Szymonski, M. Fermi level pinning at the Ge(001) surface—A case for non-standard explanation. *J. Appl. Phys.* **2015**, *118*, No. 185703.
(49) Loscutoff, P. W.; Bent, S. F. Reactivity of the germanium surface: Chemical passivation and functionalization. *Annu. Rev. Phys. Chem.* **2006**, *57*, 467−495.
(50) Scace, R. I.; Slack, G. A. Solubility of Carbon in Silicon and Germanium. *J. Chem. Phys.* **1959**, *30*, 1551−1555.
(51) Lee, J. H.; Lee, E. K.; Joo, W. J.; Jang, Y.; Kim, B. S.; Lim, J. Y.; Choi, S. H.; Ahn, S. J.; Ahn, J. R.; Park, M. H.; et al. Wafer-scale growth of single-crystal monolayer graphene on reusable hydrogen-terminated germanium. *Science* **2014**, *344*, 286−289.
(52) Cançado, L. G.; Jorio, A.; Ferreira, E. H.; Stavale, F.; Achete, C. A.; Capaz, R. B.; Moutinho, M. V.; Lombardo, A.; Kulmala, T. S.; Ferrari, A. C. Quantifying defects in graphene via Raman spectroscopy at different excitation energies. *Nano Lett.* **2011**, *11*, 3190−3196.
(53) Lucchese, M. M.; Stavale, F.; Ferreira, E. H. M.; Vilani, C.; Moutinho, M. V. O.; Capaz, R. B.; Achete, C. A.; Jorio, A. Quantifying ion-induced defects and Raman relaxation length in graphene. *Carbon* **2010**, *48*, 1592−1597.
(54) Jang, H. S.; Lim, J. Y.; Kang, S. G.; Seo, Y. M.; Moon, J. Y.; Lee, J. H.; Whang, D. Toward Scalable Growth for Single-Crystal Graphene on Polycrystalline Metal Foil. *ACS Nano* **2020**, *14*, 3141−3149.
(55) Araujo, P. T.; Terrones, M.; Dresselhaus, M. S. Defects and impurities in graphene-like materials. *Mater. Today* **2012**, *15*, 98−109.
(56) Toh, C. T.; Zhang, H.; Lin, J.; Mayorov, A. S.; Wang, Y. P.; Orofeo, C. M.; Ferry, D. B.; Andersen, H.; Kakenov, N.; Guo, Z.; et al. Synthesis and properties of free-standing monolayer amorphous carbon. *Nature* **2020**, *577*, 199−203.
(57) Kuzum, D.; Park, J.-H.; Krishnamohan, T.; Saraswat, K. C. Effect of interfacial oxide on Ge MOSCAP and N-MOSFET characteristics. *Microelectron. Eng.* **2011**, *88*, 3428−3431.
(58) Reed, J.; Fan, Z.; Gao, G. B.; Botchkarev, A.; Morkoç, H. GaAs metal insulator semiconductor capacitors and high transconductance metal insulator semiconductor field effect transistors. *Appl. Phys. Lett.* **1994**, *64*, 2706−2708.
(59) Piskorski, K.; Przewlocki, H. M. The methods to determine flat-band voltage V_{FB} in semiconductor of a MOS structure. In *Proceedings of the 33rd International Convention MIPRO*; IEEE: Opatija, Croatia, May 2010; pp 37−42.
(60) Brews, J. R.; Nicollian, E. H. Improved MOS Capacitor Measurements Using the Q-C Method. *Solid·State Electron.* **1984**, *27*, 963−975.

https://doi.org/10.1021/acsnano.4c12780
ACS Nano 2025, 19, 1056−1069

(61) Terman, L. M. An investigation of surface states at a silicon/silicon oxide interface employing metal-oxide-silicon diodes. *Solid-State Electron.* **1962**, *5*, 285−299.
(62) Nicollian, E. H.; Brews, J. R. *MOS (Metal Oxide Semiconductor) Physics and Technology*; Wiley: New York, 1982; pp 1−650.
(63) Lang, D. V. Deep-level transient spectroscopy: A new method to characterize traps in semiconductors. *J. Appl. Phys.* **1974**, *45*, 3023−3032.
(64) Neugroschel, A.; Sah, C. T.; Han, K. M.; Carroll, M. S.; Nishida, T.; Kavalieros, J. T.; Lu, Y. Direct-Current Measurements of Oxide and Interface Traps on Oxidized Silicon. *IEEE Trans. Electron Devices* **1995**, *42*, 1657−1662.
(65) Hung, K. K.; Cheng, Y. C. Characterization of Si-SiO_2 interface traps in p-metal-oxide-semiconductor structures with thin oxides by conductance technique. *J. Appl. Phys.* **1987**, *62*, 4204−4211.
(66) Akkili, V. G.; Raju, N. P.; Thangavel, R.; Srivastava, V. M. Simulation Analysis of High Field-Effect Mobility in p-Channel-Based Cylindrical Thin-Film Transistors. *J. Electron. Mater.* **2022**, *51*, 5015−5025.
(67) Ali, F.; Ahmed, F.; Taqi, M.; Mitta, S. B.; Ngo, T. D.; Eom, D. J.; Watanabe, K.; Taniguchi, T.; Kim, H.; Hwang, E.; Yoo, W. J. Traps at the hBN/WSe_2 interface and their impact on polarity transition in WSe_2. *2D Mater.* **2021**, *8*, No. 035027.
(68) Chattopadhyay, P. Capacitance technique for the determination of interface state density of metal-semiconductor contact. *Solid-State Electron.* **1996**, *39*, 1491−1493.
(69) Vais, A.; Franco, J.; Lin, H.-C.; Collaert, N.; Mocuta, A.; De Meyer, K.; Thean, A. Impact of starting measurement voltage relative to flat-band voltage position on the capacitance-voltage hysteresis and on the defect characterization of InGaAs/high-*k* metal-oxide-semiconductor stacks. *Appl. Phys. Lett.* **2015**, *107*, No. 223504.
(70) Ke, M.; Yu, X.; Zhang, R.; Kang, J.; Chang, C.; Takenaka, M.; Takagi, S. Fabrication and MOS interface properties of ALD $AlYO_3$/GeO/Ge gate stacks with plasma post oxidation. *Microelectron. Eng.* **2015**, *147*, 244−248.
(71) Ke, M.; Takenaka, M.; Takagi, S. Reduction of slow trap density of Al_2O_3/GeO_x/n-Ge MOS interfaces by inserting ultrathin Y_2O_3 interfacial layers. *Microelectron. Eng.* **2017**, *178*, 132−136.
(72) Franco, J.; Kaczer, B.; Roussel, J., Ph.; Mitard, J.; Sioncke, S.; Witters, L.; Mertens, H.; Grasser, T.; Groeseneken, G. Understanding the Suppressed Charge Trapping in Relaxed- and Strained-Ge/SiO_2/HfO_2 pMOSFETs and Implications for the Screening of Alternative High-Mobility Substrate/Dielectric CMOS Gate Stacks. In *Proceedings of the IEEE International Electron Devices Meeting (IEDM)*, Washington, DC, USA, December 2013; pp 15.2.1−15.2.4.
(73) Di Bartolomeo, A.; Genovese, L.; Giubileo, F.; Iemmo, L.; Luongo, G.; Foller, T.; Schleberger, M. Hysteresis in the transfer characteristics of MoS_2 transistors. *2D Mater.* **2018**, *5*, No. 015014.
(74) Lundström, I.; Christensson, S.; Svensson, C. Carrier trapping hysteresis in MOS transistors. *Phys. Stat. Sol. (a)* **1970**, *1*, 395−407.
(75) Firdaus, H.; Watanabe, T.; Hori, M.; Moraru, D.; Takahashi, Y.; Fujiwara, A.; Ono, Y. Electron aspirator using electron-electron scattering in nanoscale silicon. *Nat. Commun.* **2018**, *9*, No. 4813.
(76) Groeseneken, G.; Franco, J.; Cho, M.; Kaczer, B.; Toledano-Luque, M.; Roussel, P.; Kauerauf, T.; Alian, A.; Mitard, J.; Arimura, H.; Lin, D.; Waldron, N.; Sioncke, S.; Witters, L.; Mertens, H.; Ragnarsson, L.-Å.; Heyns, M.; Collaert, N.; Thean, A.; Steegen, A. BTI Reliability of Advanced Gate Stacks for Beyond-Silicon Devices: Challenges and Opportunities. In *Proceedings of the IEEE International Electron Devices Meeting (IEDM)*, San Francisco, CA, USA, December 2014; pp 34.4.1−34.4.4.
(77) Lin, J.; Gomeniuk, Y. Y.; Monaghan, S.; Povey, I. M.; Cherkaoui, K.; O'Connor, É.; Power, M.; Hurley, P. K. An investigation of capacitance-voltage hysteresis in metal/high-*k*/$In_{0.53}Ga_{0.47}As$ metal-oxide-semiconductor capacitors. *J. Appl. Phys.* **2013**, *114*, No. 144105.
(78) Wan, H. W.; Hong, Y. J.; Cheng, Y. T.; Hong, M.; Kwo, J.BTI Characterization of MBE Si-Capped Ge Gate Stack and Defect Reduction via Forming Gas Annealing. In *Proceedings of the IEEE International Reliability Physics Symposium (IRPS)*, Monterey, CA, USA, March 2019; pp 1−6.
(79) Kim, W.-H.; Shin, K.; Shong, B.; Godet, L.; Bent, S. F. Atomic Layer Deposition of Pt on the Surface Deactivated by Fluorocarbon Implantation: Investigation of the Growth Mechanism. *Chem. Mater.* **2020**, *32*, 9696−9703.
(80) Mannhar, J.; Herrnberger, A. The interface is still the device. *Nat. Mater.* **2012**, *11*, 91 DOI: 10.1038/nmat3244.
(81) Kresse, G.; Hafner, J. Ab initio molecular-dynamics simulation of the liquid-metal-amorphous-semiconductor transition in germanium. *Phys. Rev. B* **1994**, *49*, 14251−14269.
(82) Perdew, J. P.; Burke, K.; Ernzerhof, M. Generalized gradient approximation made simple. *Phys. Rev. Lett.* **1996**, *77*, 3865−3868.
(83) Zhang, Y. K.; Yang, W. T. Comment on ″Generalized gradient approximation made simple. *Phys. Rev. Lett.* **1998**, *80*, 890.
(84) Perdew, J. P.; Ernzerhof, M.; Burke, K. Rationale for mixing exact exchange with density functional approximations. *J. Chem. Phys.* **1996**, *105*, 9982−9985.
(85) Adamo, C.; Barone, V. Toward reliable density functional methods without adjustable parameters: The PBE0 model. *J. Chem. Phys.* **1999**, *110*, 6158−6170.

https://doi.org/10.1021/acsnano.4c12780
ACS Nano 2025, 19, 1056−1069